MODELLING CLOSED-DIE FORGING OPERATIONS USING TOTAL LAGRANGIAN SMOOTH PARTICLE HYDRODYNAMICS

A PREPRINT

A. C. Manson

Sep. 21, 2019

ABSTRACT

Total Lagrangian Smooth Particle Hydrodynamics (TLSPH) has been applied to a set of non-trivial, commercially interesting forging examples. Being a mesh-free method, TLSPH can conveniently simulate processes having large deformation and material separation. Test cases were designed that were characterized by large material flows having large changes in grain connectivity. The implementation used, Smooth Mach Dynamics (SMD), provided tunable simulation parameters that enabled the simulation to optimally match each case. The results showed that the TLSPH/SMD has the potential to model the metal forging process efficiently without numerical instabilities. Each case studied required adaptation of the simulation parameters to optimize the results.

1 Introduction

1.1 Motivation

Forging is an important manufacturing operation because it is economical and produces parts having high strength, toughness, and ductility as a result of the control of grain formation and orientation. The motivation for forging simulation is to predict the outcome of each stage of the forging workflow in order to mitigate problems such as:

- incomplete die filling
- production and cracking of flash
- undesirable grain structure
- cold shuts
- fracture during forging
- excessive required forging pressures
- high residual stress
- poor billet design
- undesirable material flow
- excess operations needed to create a part

Ability to predict these outcomes can help optimize the design of preform dies, forging operations and process changes such as alterations of billet temperature and subsequent heat treatment operations.

1.2 Background

Understanding material deformation and flow patterns during forging can provide key insights to the design of forging operations. Forging defects can lead to premature failure of structures. Predicting the generation of defects will allow forging operations to be optimized.

Forging processes are characterised by rapid deformations under large forces that result in large plastic deformations. When the conventional finite element methods (FEM) are used to model large strain problems, high deformation inevitably leads to mesh distortion and possible instability in the simulation because the topology and shape of the elements have profound effects on the quality and accuracy of FE solutions [1]. Severely distorted elements may even lead to a singular stiffness matrix (non-positive Jacobian) and consequent analysis failure [2]. These issues are compounded in forging simulations, where very high displacements may produce mesh inter-penetration and entanglement resulting in the loss of connectivity and topological integrity of the finite element network. In such cases, re-meshing part or all of the geometry is the only alternative solution.

A mesh-less method, such as spherical particle hydrodynamics (SPH), offers many advantages for modelling continuous high deformation processes such as forging. SPH is a particle based numerical method for solving partial differential equations. The problem geometry is idealized into 'particles' that represent specific material volumes. The method uses a local interpolation from the neighboring particles to construct continuous field approximations that can be used to discretise the problem space. Even though SPH has been traditionally used for mod-

elling fluid flows, SPH has been adapted to a wide variety of solid mechanics problems [3]. Since SPH does not require an explicit grid or mesh structure to represent the problem geometry it eliminates time-consuming effort of mesh generation and refinement through an implicit mechanism. It also avoids the need to address the difficulties associated with traditional mesh-based methods in maintaining the integrity and quality of the mesh under large deformations thereby reducing associated errors. The grid-free nature of SPH makes this method ideally suited to modelling material forging processes that involve large deformations and changes in topological connectivity. Moreover, SPH intrinsically handles surface contacts during forging and naturally predicts self-contacts.

To address the specific needs of solid mechanics, the total-Lagrangian SPH (TLSPH) was devised [4, 5]. In order for TLSPH to be viable, several problems had to be solved [6] to ensure its convergence and stability in order that large deformations having plastic flow could be accurately simulated [6]. In lieu of explicity remeshing, TLSPH handles remeshing implicitly by resetting of the material reference frame in response to a displacement metric. The implementation used in this study was implemented and packaged within the Lammps simulation platform [7] as the package USER-SMD.

1.3 Outline

The paper will review the theory associated with the TLSPH method, discuss the simulation method and related parameters, introduce the four forging case studies, present the results of these simulations and finally discuss issues found during the study.

2 Materials and Methods

2.1 Theory

The conservation equations will be solved by means of a total-Lagrangian approach which uses a reference configuration to compute stresses and accelerations. Both conservation and constitutive equations are expressed in terms of the reference coordinates X, which are taken to be the coordinates of the initial, undeformed configuration. A mapping between the two systems describes the motion at time t:

$$\mathbf{x} = \phi(\mathbf{X}, t). \tag{1}$$

The displacement u (relative to the reference configuration $\mathbf{X}$) is given by:

$$\mathbf{u} = \mathbf{x} - \mathbf{X}. \tag{2}$$

The associated deformation gradient is given by:

$$\mathbf{F} = \frac{d\mathbf{x}}{d\mathbf{X}} = \frac{d\mathbf{u}}{d\mathbf{X}} + \mathbf{I}. \tag{3}$$

which is the transformation matrix that describes the rotation and stretch relative to the reference configuration.

The equations for mass, impulse, and energy conservation are given by:

$$\begin{aligned} \rho J &= \rho_0 \\ \mathbf{u} &= \frac{1}{\rho_0} \nabla_0 \cdot \mathbf{P}^T \\ \dot{e} &= \frac{1}{\rho_0} \dot{\mathbf{F}} : \mathbf{P} \end{aligned} \tag{4}$$

here, ρ is the mass density, $\mathbf{P}$ the first Piola–Kirchhoff stress tensor, e is the internal energy, and ∇ is the gradient or divergence operator and symbol T denotes the transpose of a matrix. The subscript 0 refers to a quantity evaluated in the reference configuration, while the absence of this subscript means that the current configuration is to be used. J is the determinant of the deformation gradient $\mathbf{F}$.

2.1.1 Total Lagrangian SPH Formulation

In the SPH numerical method, the interpolated value of a function A at any position $\mathbf{x}$ can be calculated from the discrete values A_j on the surrounding particles by:

$$A(\mathbf{x}) = \sum_{j:\, |\mathbf{x}-\mathbf{x}_j|<2h} V_j A_j W(\mathbf{x} - \mathbf{x}_j, h) \tag{5}$$

Here, the sum is over all particles j within a radius $2h$ of $\mathbf{x}$. $W(\mathbf{x}, h)$ is a spline based interpolation or smoothing kernel with radius $2h$ and V_j is the volume fraction of the support particle j.

At the beginning of each time step, a shape matrix

$$\mathbf{K}_i = \sum_{j \in S_i} V_j^0 \nabla W_i(X_{ij}) \otimes (\mathbf{X}_j - \mathbf{X}_i). \tag{6}$$

is computed as the sum of the dyadic product of two vectors, $\nabla W_i(X_{ij})$, the gradient of the kernel function and $\mathbf{X}_j - \mathbf{X}_i$, the displacement of support particle j relative to particle i in the reference (ie. material) configuration. Here, $W_i(X_{ij})$ is a kernel function which depends only on the scalar distance between particles i and j. V_j denotes the supporting particle volume, and S_i the support region of the particle i. The shape matrix reflects the distribution of the particles in the support region surrounding the particle i within the reference configuration and is used to normalize the deformation to a spherical shape so that first order consistency is maintained. This constraint is expressed:

$$\sum_{j \in S_i} V_j^0 (\mathbf{X}_j - \mathbf{X}_i) \otimes \nabla W_i(X_{ij}) = \mathbf{I} \tag{7}$$

The deformation gradient and its time derivative are then obtained as:

$$\mathbf{F}_i = \sum_{j \in S_i} V_j^0 (\mathbf{x}_j - \mathbf{x}_i) \otimes \mathbf{K}^{-1} \nabla W_i(X_{ij}). \tag{8}$$

$$\dot{\mathbf{F}}_i = \sum_{j \in S_i} V_j^0 (\mathbf{v}_j - \mathbf{v}_i) \otimes \mathbf{K}^{-1} \nabla W_i(X_{ij}). \tag{9}$$

where $\mathbf{x}$ and $\mathbf{v}$ are the coordinates and velocities in the current configuration. The velocity gradient in the current configuration is then obtained as $\mathbf{L}_i \leftarrow \dot{\mathbf{F}}_i \mathbf{F}_i^{-1}$. The Cauchy stress σ is ultimately obtained by time integration of a constitutive model which relates the Cauchy stress rate to the strain rate tensor $\mathbf{D}_i \leftarrow \frac{1}{2}(\mathbf{L}_i + \mathbf{L}_i^T)$.

To obtain the Cauchy stress, one first needs the polar decomposition of the deformation gradient $\mathbf{F}$:

$$\mathbf{R}_i \mathbf{U}_i = \mathbf{F}_i \tag{10}$$

which is used to remove the rigid rotation from the strain rate tensor:

$$\mathbf{d}_i = \mathbf{R}_i^T \mathbf{D}_i \mathbf{R}_i \tag{11}$$

From there, one can then use the constitutive relations to calculate the Cauchy stress σ_i.

The first Piola–Kirchhoff stress, $\mathbf{P}_i = J\sigma_i \mathbf{F}_i^{-T}$ is used to link the material frame to the current frame where the deformation related forces are calculated as:

$$\begin{aligned}\mathbf{f}_i^d = \sum_{j \in S_i} V_j^0 V_i^0 (&\mathbf{P}_i \mathbf{K}_i^{-1} \nabla W_i(X_{ij}) \\ &- \mathbf{P}_j \mathbf{K}_j^{-1} \nabla W_j(X_{ji})).\end{aligned} \tag{12}$$

In addition to the deformation related force, there is a viscous force which becomes significant at higher velocities. This is given as:

$$\mathbf{f}_i^v = \sum_{j \in S_i} m_j m_i \Pi_{ij} \mathbf{I} \cdot \nabla W_i(X_{ij}) \tag{13}$$

where

$$\Pi_{ij} = \begin{cases} \frac{-\alpha c_{ij} \eta_{ij} + \beta \eta_{ij}^2}{\rho_{ij},} & (\mathbf{v}_i - \mathbf{v}_j) \cdot (\mathbf{x}_i - \mathbf{x}_j) < 0, \\ 0, & \text{else.} \end{cases} \tag{14}$$

where $\eta_{ij} = \frac{h(\mathbf{v}_i - \mathbf{v}_j) \cdot (\mathbf{x}_i - \mathbf{x}_j)}{|\mathbf{x}_i - \mathbf{x}_j|^2}$, $\rho_{ij} = \frac{\rho_i + \rho_j}{2}$, c_{ij} the speed of sound between particles i and j, and α, β the shear and bulk viscosities respectively. Finally, the net force acting on particle i is:

$$\mathbf{f}_i = \mathbf{f}_i^d + \mathbf{f}_i^v \tag{15}$$

2.1.2 Hourglass Control

Within the region neighboring any given particle, a degeneracy of zero energy motions can occur, the so-called hourglass effect. To eliminate this effect, an ideal particle separation based on the initial configuration is proposed:

$$\langle \mathbf{x}_{ij} \rangle^i = \mathbf{F}_i \mathbf{X}_{ij} \tag{16}$$

As the particles deviate from this ideal separation, a corrective force can be applied. This corrective force is designed to minimize the error metric:

$$\begin{aligned}\varepsilon_{ij} &= \frac{1}{2}\left(\langle \mathbf{x}_{ij} \rangle^i - \mathbf{x}_{ij} + \langle \mathbf{x}_{ij} \rangle^j - \mathbf{x}_{ij} \right) \\ &= \frac{1}{2}(\mathbf{F}_i + \mathbf{F}_j)\mathbf{X}_{ij} - \mathbf{x}_{ij}\end{aligned} \tag{17}$$

To enforce the hourglass condition and maintain proper angular momentum, the corrective force:

$$\mathbf{f}_i^{HG} = -\xi \sum_{j \in S_i} V_j^0 V_i^0 W(X_{ij}) \varepsilon_{ij} \frac{\varepsilon_{ij} \cdot \mathbf{x}_{ij}}{\mathbf{x}_{ij}^2} \frac{\mathbf{x}_{ij}}{x_{ij}}. \tag{18}$$

is applied.

2.1.3 Constitutive Model

The stress is broken into its pressure p and deviatoric $\sigma_{\mathbf{d}}$ components.

$$\sigma = p\mathbf{I} + \sigma_{\mathbf{d}}. \tag{19}$$

The shear modulus for an isotropic material is given as:

$$S = \frac{E}{2(1+\nu)}. \tag{20}$$

In this study, a simple piecewise linear constitutive model is used where stress varies linearly with strain up to the yield point (in proportion with the elastic modulus) and varies linearly past the yield point (in proportion to the strain hardening modulus).

2.1.4 Plasticity Model

The radial return algorithm of Wilkins [8] is used to calculate the elastoplastic deformation. A trial deviatoric stress is first calculated assuming an initial elastic response. This gives an increment in plastic strain:

$$\Delta\epsilon^p = \frac{\sigma_{vm} - \sigma_y}{3G + H} \tag{21}$$

Here, σ_{vm} is the von Mises stress and σ_y is the current yield stress. The increment in the plastic strain is:

$$\epsilon^p(t + \Delta t) = \epsilon^p(t) + \Delta\epsilon^p \tag{22}$$

The yield stress increment is given as:

$$\Delta\sigma_y = H\Delta\epsilon^p \tag{23}$$

where H is the hardening modulus. The updated deviatoric stress σ_d is given by:

$$\sigma_d(t + \Delta t) = r_s \sigma_d(t) \tag{24}$$

where r_s is the radial scale factor given as:

$$r_s = \frac{\sigma_y}{\sigma_{vm}} \tag{25}$$

2.1.5 Algorithm

The algorithm for describing the stress driven motion of SMD particles given in [9] is given in Appendix A containing the steps to reset the material reference frame along with the radial return algorithm used to handle plastic deformation [9].

2.2 Forging Cases

The test cases have been chosen to address select problem areas mentioned in the introduction such as die filling and fracture. The simplest billet geometries (blocks, cylinders) were chosen to simplify the interpretation of material flow patterns.

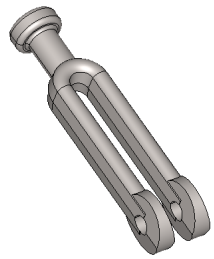

(a) Part

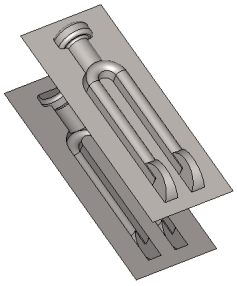

(b) Die

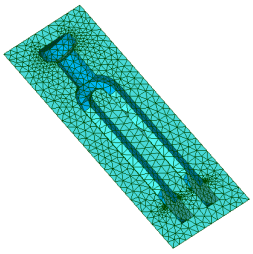

(c) Mesh Lower Die

Figure 1: Yoke: a: part, b: die, c: lower die mesh

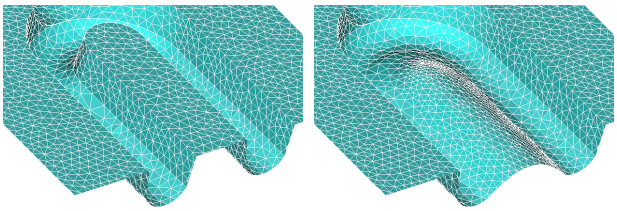

(a) Finish die (b) Preform die

Figure 2: Smoothing applied to yoke die mesh central section.

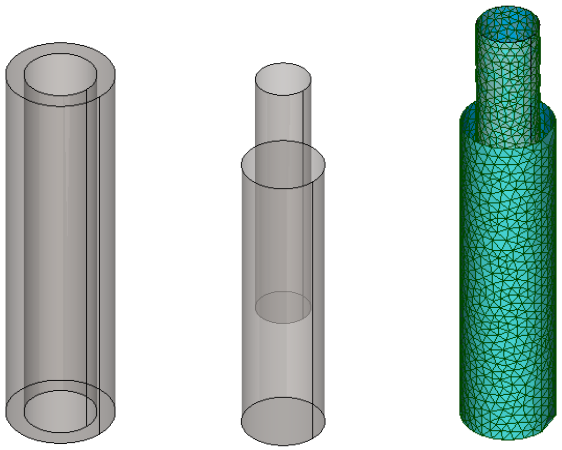

(a) Part (b) Die (c) Die Mesh

Figure 3: Reverse Extrusion of Seamless Pipe: a: Part, b: Die, c: Die mesh

2.2.1 Sliding Yoke

The sliding yoke was chosen due to its non-trivial topology and variation in depth and breadth along its long dimension. The regions between the legs of the yoke and around the slider pin are expected to be regions of high shear. Here, the particle topology will change and require a reset of the reference state.

The part is forged normal to its thickness (the smallest dimension), similar to an engine connecting rod and forged from a rectangular billet with a volume slightly larger than the part itself to allow for complete die filling. The billet is oriented lengthwise to the part and has a width slightly smaller than the part itself. The center of the finish die has a raised region that forms the space between the legs of the yoke fig. 2a. Preliminary simulations showed that this feature would cause an excessive separation (ie. fracture) of the billet away from the die cavity toward the flash region of the die. To address this, the hollowed section was smoothed to create a preform die fig. 2b.

2.2.2 Seamless Pipe (Reverse Extrusion)

The seamless pipe is awkward to model using FEM techniques due to the continuous changes in grain topology at the shear zone near the outer edge of the punch. The meshless approach eliminates these remeshing steps.

The die was modeled as two concentric cylinders, each open at one end fig. 3. The billet is cylindrical and the forging path along the axis of the two die cylinders. As the forging progresses, material is compressed and initially displaced outward followed by flow in the opposite direction of the punch motion. Preliminary simulations showed that a preform die was not neccesary.

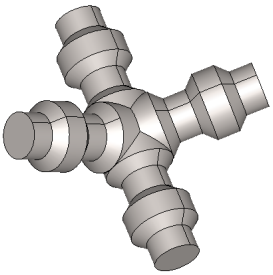

(a) Part

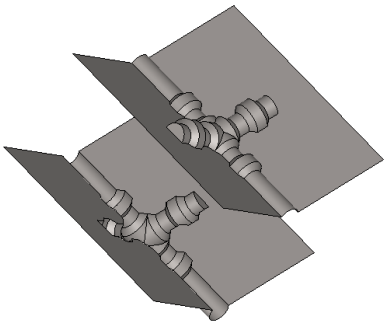

(b) Die

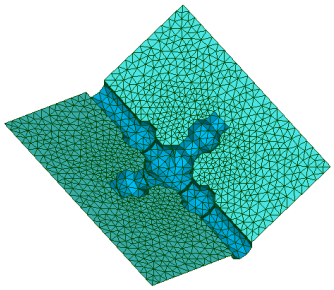

(c) Lower Mesh Die

Figure 4: 4arm part: a: part, b: die, c: die mesh

2.2.3 Four arm offset joint

This part, fig. 4, is similar to a part modeled in previously [10] and will be reproduced for consistency. It is expected to exhibit frequent particle topology changes along with non-trivial material flows. As the material navigates the constricted and expanding regions, one expects perturbations in velocity and flowrate.

The combined two punch motion is collinear with the two aligned arms of the part fig. 4b. The operation requires the closure of the upper and lower die sections followed by the two cylindrical punches sliding toward the center. In this case one is expected to initially see compression along the long axis of the cylindrical billet. As the two punches move toward each other, the billet will buckle and fill the two orthogonal arms of the die.

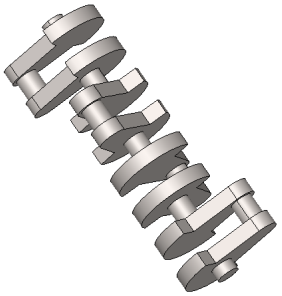

(a) Part

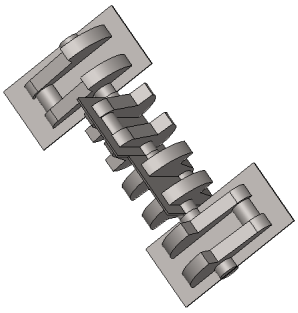

(b) Compound Die

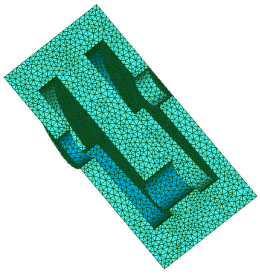

(c) Crank Unit Die Mesh

Figure 5: crossplane crankshaft part: a: part, b: die, c: die mesh

2.2.4 Crankshaft Unit

This case has similarities to the yoke case, but with a wider variation of thickness in the direction of the punch motion. As a result, it can test the extent of die filling as a function of initial billet placement.

A cross plane crankshaft can be forged using a compound die with two forging planes oriented at right angles fig. 5b. Each plane has two die units each shaping a single crank throw. To handle the cross plane case, a full length billet stradling each crank across the main bearings is needed, otherwise one would rely on the fusion of pairs of oxidized surfaces. The construction of this billet will be addressed in later work.

Each crankshaft throw has a large depth variation and is expected to produce large material deformations fig. 6. The action of the forging press is along the shortest dimension of the part ie. normal to the plane of the crank

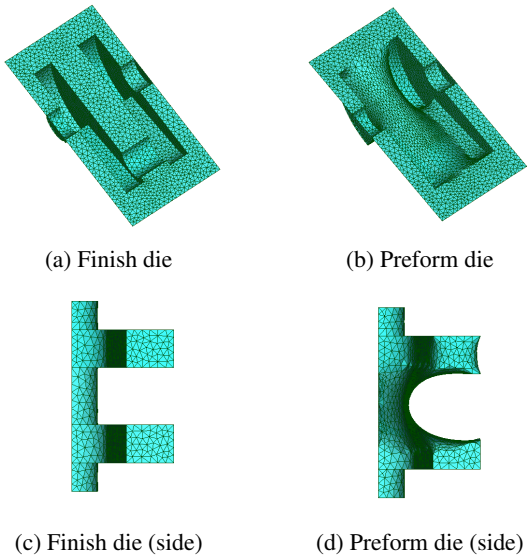

(a) Finish die (b) Preform die

(c) Finish die (side) (d) Preform die (side)

Figure 6: Comparison of finish die and preform die.

throw. Due to the large hollowed out section in the center of the crank throw, a preform die, similar to the yoke case, is employed fig. 6d.

2.3 Simulation Strategy

Each part and and its corresponding die geometry was modeled and meshed using SALOME [11] and the die meshs exported as .stl files describing a 2D triangular surface mesh. The forging simulation was done using Lammps [7] with the SMD user package [9]. Each simulation instance had a corresponding Lammps script file where the material, simulation parameters and simulation control logic were defined. The die geometry was imported to Lammps and the billet geometry defined within Lammps itself. The material used was steel at different temperatures: three cases at room temperature and the 4arm case at $1000°C$. During each trajectory, the positions, velocities and relevant SMD properties (such as stress and strain) were written to a Lammps dump file. Other properties such as punch displacement and punch reaction force were computed and written out to data files to be graphed. Initial parameter settings and billet sizes were adjusted according to any issues that occured during the simulation. The volume of the part was used to estimate the initial billet size. The billet geometry was matched to the die geometry as closely as possible to prevent excess flash. In two cases, preform dies were modeled to address problematic material flows observed when finish dies were directly applied to the raw billet. This work will report the simulation of the preform dies since this is where most of the deformation occured.

Material Parameters	
Parameter (units)	**Description**
E (GPa)	Youngs Modulus
σ_y (GPa)	Yield Stress
ρ_0 (kg/mm^3)	Initial density
ν	Poissons ratio
H (GPa)	Strain hardening modulus

Table 1: Definition of Material Parameters.

Material Parameters by Case				
Parameter	Yoke	Pipe	4arm	crank
E	210	210	9	210
σ_y	0.5	0.5	0.023	0.5
ρ_0	7.7e-6	7.7e-6	7.7e-6	7.7e-6
ν	0.3	0.3	0.3	0.3
H	0.002	0.002	0.002	0.002

Table 2: Material Parameters used in each forging case.

2.4 Simulation Platform and Parameters

2.4.1 Material Parameters

Table 1 identifies the relevant material parameters. Here, steel was used where the modulus of elasticity and the yield stress varied with temperature according to [12]. Table 2 provides the material parameters by case.

2.4.2 Simulation Parameters

A set of tunable SMD parameters were used to control aspects of the simulation. These parameters are defined in tab. 3 and the settings given, by case, in tab. 4.

2.5 Presentation of results

The results are generated from the simulation trajectories using the Open Visualization Toolkit (OVITO) [13] and typically show the evolution of deformation and other parameters in space and time for each case. In the figures to follow, rainbow color coding is used where blue hues indicate a lower value while red hues indicate a higher value. For instance, strain values will vary within the range $[-1.0 \rightarrow 1.0]$ with the negative values being blue

SMD Simulation Parameters	
Parameter (units)	**Description**
$q1$	Artificial Viscosity
l_0 (mm)	Particle Size
Hg	Hourglass Coefficient
skr	Smoothing Kernel Radius Multiplier
up	Update Parameter
E_c (GPa)	Contact Stiffness
H_p	Hertz Parameter

Table 3: Simulation Parameter Definitions.

Simulation Parameters by Case				
Parameter	Yoke	Pipe	4arm	crank
$q1$	0.6	0.6	1.0	0.6
$\mathbf{l}_0$	0.3	0.2	0.3	0.4
Hg	10	10	10	10
skr	2.01	2.01	2.01	2.01
up	0.3	0.5	0.4	NA
E_c	80.0	80.0	80.0	80.0
H_p	1.0	1.0	0.8	1.0

Table 4: Simulation Parameters by Case.

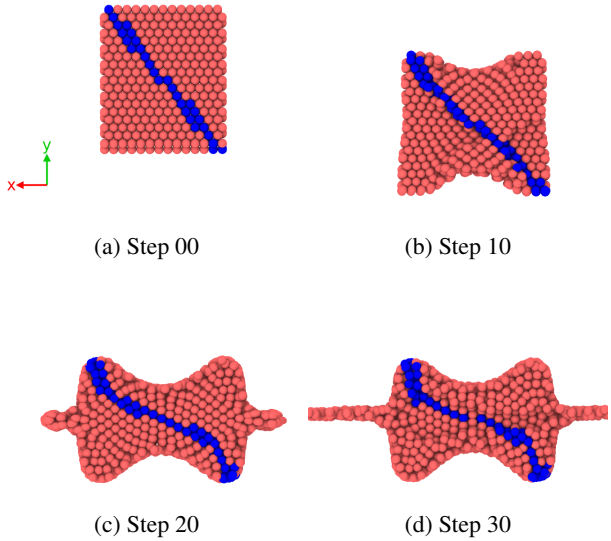

(a) Step 00 (b) Step 10

(c) Step 20 (d) Step 30

Figure 7: Evolution of rectangular layer through mid-section of yoke.

and the positive values being red. Unless the coloring is obvious, the range of values for the hues is given for each figure or subfigure. Data is typically dumped from Lammps every 200 time steps. The notation m/n indicates snapshot m out of n total snapshots.

3 Results

3.1 Sliding Yoke

3.1.1 Preform Die

The yoke system showed good die filling with a reasonable amount of flash. A lateral cross section about midway along the legs of the yoke fig. 1a was featured with respect to particle deformation and other properties. The evolution of a diagonal layer of particles was followed in fig. 7. The trajectory showed that the outer diagonal would align with the legs of the yoke and the center diagonal would flatten out fig. 7d. As the die closes, the orientation/elongation of the particles at the die surface becomes apparent.

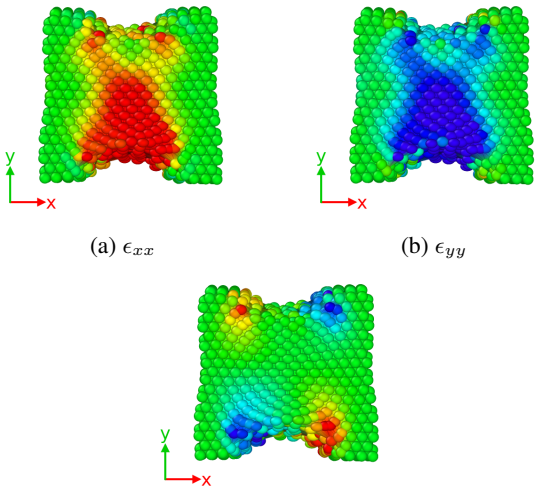

(a) ϵ_{xx} (b) ϵ_{yy}

(c) ϵ_{xy}

Figure 8: Sectional strains time 14/31: [-0.1 $\rightarrow$ 0.1].

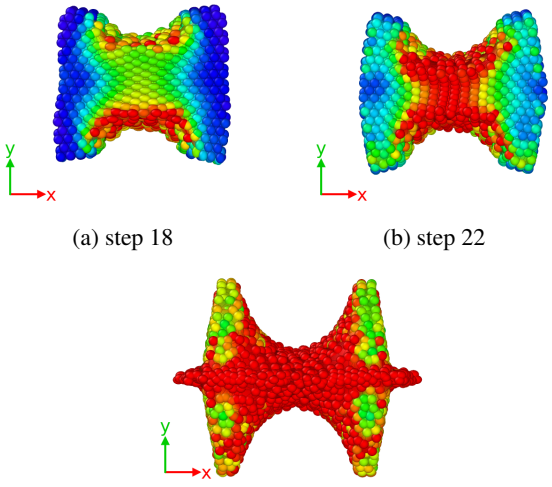

(a) step 18 (b) step 22

(c) step 29

Figure 9: Evolution of plastic strain rate: [0 $\rightarrow$ 18].

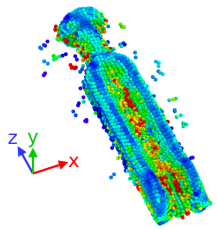

(a) ϵ_{xx}: [-0.1 → 0.1]

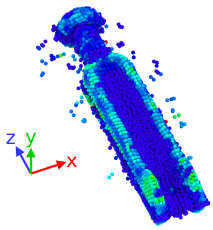

(b) ϵ_{yy}: [-0.1 → 0.1]

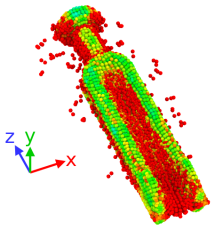

(c) Plastic flow: [0 → 20]

Figure 10: Properties at final state.

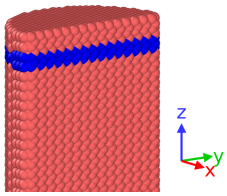

(a) Step 00

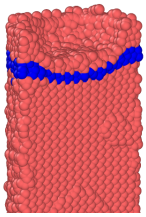

(b) Step 10

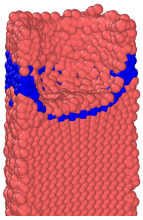

(c) Step 20

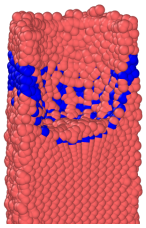

(d) Step 50

Figure 12: Evolution of cylindrical layer during reverse extrusion.

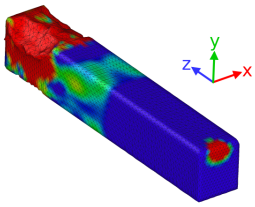

(a) Time 2/31

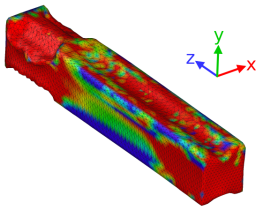

(b) Time 10/31

Figure 11: Von Mises stress: [0 → 0.5].

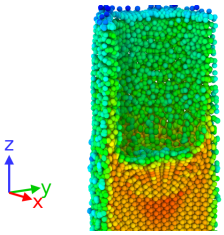

(a) Neighbors: [0 → 55]

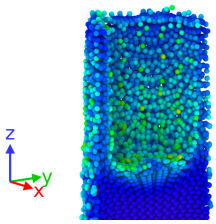

(b) Plastic Strain: [0 → 5]

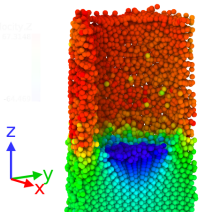

(c) v_z: [-10 → 10]

Figure 13: Properties at 30% extrusion.

The sectional strain is shown in fig. 8 at an intermediate stage of the forging process. The lateral strain ϵ_{xx} is maximized near the midline of the billet where the central region is being carved out. The vertical strain ϵ_{yy} is minimized near the midline of the billet. The shear ϵ_{yx} zone appears at the corners where the central die section displaces the region between the yoke legs.

The plastic strain rate fig. 9 is also maximized in this central region where material is being displaced toward the sides. Initially it is concentrated at the surface and then spreads ubiquitously throughout the part as the die reaches the bottom of its stroke fig. 9. As the upper die descends, the strain rate increases on the lower billet as it is pressed against the lower die fig. 9a. From there the strain rate spreads throughout the billet and becomes confined to the midline 9b. As the base of the forging stroke is reached, the strain rate distributes throughout as the billet completely fills the die cavity fig. 9c.

The global distribution of properties is shown in fig. 10. The strain ϵ_{xx}, normal to the major axis, given in fig. 10a, shows highest strain in the region between the legs of the yoke as the material is displaced to fill the legs of the part. The strain ϵ_{yy}, in the direction of the punch motion, shows a maximum at the center of each leg. Plastic flow is maximized in the region between the yoke legs and in the region outward from the hanger pin where the flash is expected to form in the final stages of the punch motion fig. 10c.

Figure 11 shows the Von Mises stress in the early stages of the forging process. The red hue corresponds to the yield stress of the material. Initially, yield stress values are confined to the region near the pin fig. 11a but expand to the entire part fig. 11b as forging progresses.

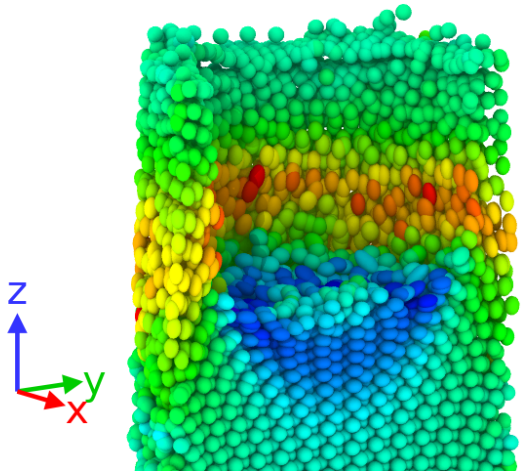

Figure 14: Grain orientation indicated by orientation of ellipsoid. Grain structure colored by ϵ_{zz}. Clipping plane normal to x axis.

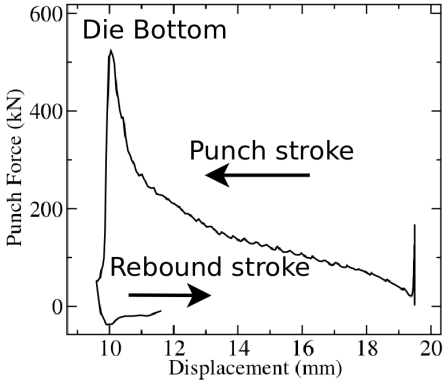

Figure 15: Force vs Displacement Forging Stages

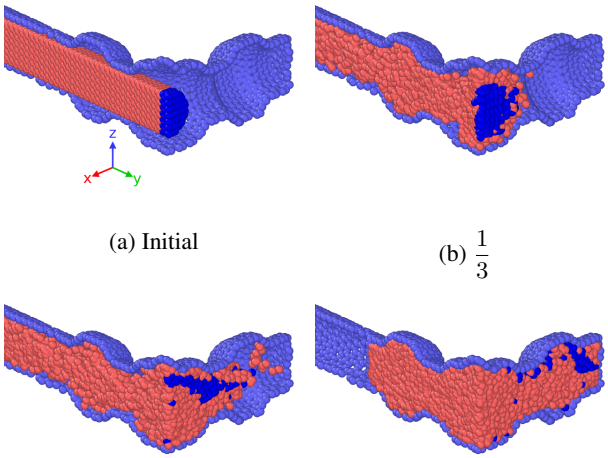

(a) Initial (b) $\frac{1}{3}$ (c) $\frac{2}{3}$ (d) Final

Figure 16: Evolution of cylindrical slice in one quadrant of the 4arm die in thirds of trajectory.

3.2 Reverse Extrusion of Seamless Pipe

The evolution of a cylindrical material layer in the seamless pipe is shown in fig. 12. The layer is compressed and squeezed outward and then upward along the outer part of the die cylinder fig. 12d. The divergence of the grains from the center can be easily seen, fig. 12, as the material is displaced outward.

Figure 13 shows the evolution of selected properties at about 30 per cent of the punch motion. The nearest neighbor plot depicts the expected higher number of neighbors toward the center and the lower number of neighbors in the extruded pipe region 13a. The plastic strain plot fig. 13b shows maximum plasticity on the inner and outer surfaces of the extruded pipe as expected. The velocity v_z in fig. 13c shows the particles below the punch moving in a downward direction and those above the punch, on the outer extruded section, moving upward at nearly the same speed. The regions well below and to the outside of the punch motion show neutral motion.

The SMD implementation computes the shape and orientation of each particle fig. 14. This information allows the structure of the particle grains and their orientation to be rendered as an ellipse. In fig. 14 one sees the grains below the punch being compressed while those on the extruded pipe walls being elongated and aligned with the die wall.

Force vs displacement is shown in fig. 15. In the early stages there is a spike in force as the material is upset. As the punch descends the force increases and near the bottom there is a notable upward inflection where the last bit of material is squeezed out. The force becomes slightly negative as the punch rebounds.

3.3 Four Armed Extrusion

To visualize the results for the four arm part, two clipping planes (at right angles) are used to carve out a quadrant of the extrusion process fig. 16, showing the axial and lateral cross sectional evolution of the billet. The die is shown in a purple color to indicate the boundary of material flow fig. 16. The initial stages of extrusion exhibit a buckling phase as the billet is longitudinally compressed (not shown). This compression gives way to the lateral plastic flow of material into the lateral arms of the die fig. 16b. As the material flows through the constricted regions, the billet narrows fig. 16c. Eventually the material fills the die cavity fig. 16d.

The spatial-temporal distributions of selected billet properties are shown in fig. 17. The strain along the punch axis fig. 17a and the associated particle velocity fig. 17b indicate peak values in the constricted regions and lower

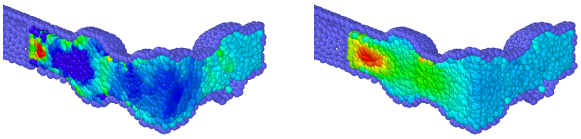

(a) ϵ_{yy}: [-0.1 → 0.1]
step 193

(b) v_y: [0 → 0.1]
step 199

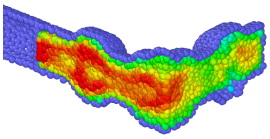

(c) Neighbors: [0 → 55]
step 199

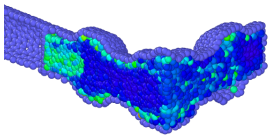

(d) Plasticity rate: [0 → 3]
step 204

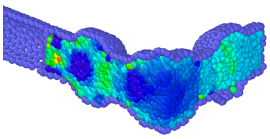

(e) Shape Y: [0.1 → 0.3]
step 206

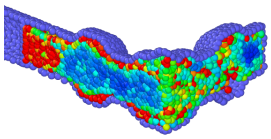

(f) Plasticity: [0 → 10]
step 187

Figure 17: Relative properties in quadrant of 4arm die.

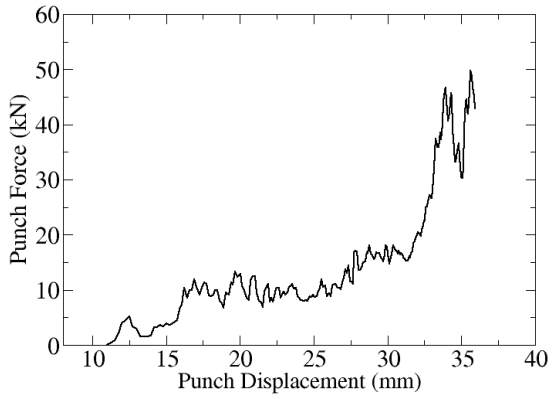

Figure 18: Force vs Displacement 4arm part

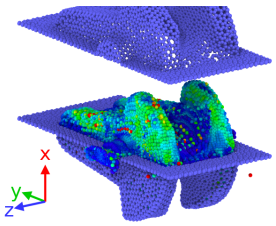

(a) ϵ_{xx}: [-0.1 → 0.1]
Step 125

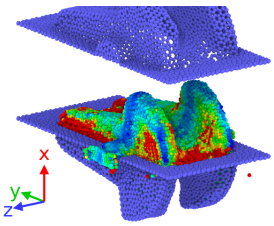

(b) ϵ_{yy}: [-0.1 → 0.1]
Step 125

Figure 19: Final ϵ_{xx}, ϵ_{yy} of crank throw shown within preform die.

values where the radius of the part increases. In the lateral arms, v_y and ϵ_{yy} become more uniform in the direction of flow normal to the puch axis.

The nearest neighbor plot fig. 17c shows highest values at the center of the die as expected, but also shows a decrease in the center regions where the die has a larger radius, probably due to the expansion as material flows into these regions. The plasticity rate fig. 17d is maximized at the entrance to the die and at its outer surface, areas of flow expansion and high shear respectively. This is expected as the snapshot is taken late in the forging process as the material is filling out the die. The y-axis aligned grain orientation fig. 17e depicts how the particles are aligned with the punch axis. Grain alignment is maximized in the constricted regions and near the outer surface of the die. The plasticity fig. 17f correlates well with the plasticity rate. It is seen to be more coherent along the punch axis and conversely in the lateral directed die arm.

The force vs displacement is shown in fig. 18. In comparison to the seamless pipe extrusion fig. 15, it appears to be more noisy. The forging process is characterized by stages that result in non-uniform flows such as when material is expanding into thicker regions or where it is buckling just prior to changing direction. Once these bottlenecks were overcome, the punch force decreased. In the latter extrusion phases, the force increases to allow the material to fill the die cavity fully.

3.4 Cross Plane Crankshaft (Unit)

3.4.1 Preform Die

The forged crankunit is shown in the context of the die mesh surface fig. 19. The strain in the direction of die motion is shown in fig. 19a and the strain in the direction of the longest part dimension in fig. 19b. The strain, ϵ_{xx}, is maximized at the counterweights opposite to the connecting rod bearing whereas the strain, ϵ_{yy}, is maximized toward the rod bearing. This is expected because the material will tend to flow in the direction normal to the punch motion in the shallower part of the die cavity.

The evolution of a billet layer (normal to the punch motion) is shown in fig. 20. The billet is shown with a

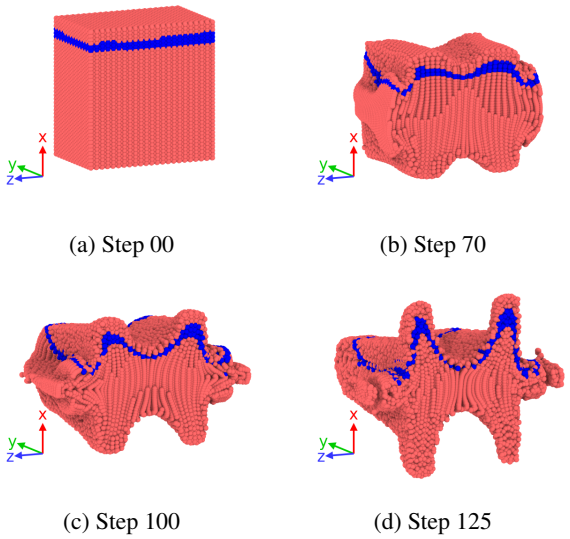

(a) Step 00 (b) Step 70

(c) Step 100 (d) Step 125

Figure 20: Evolution of layer of billet in thickest cross section (slight oblique view angle).

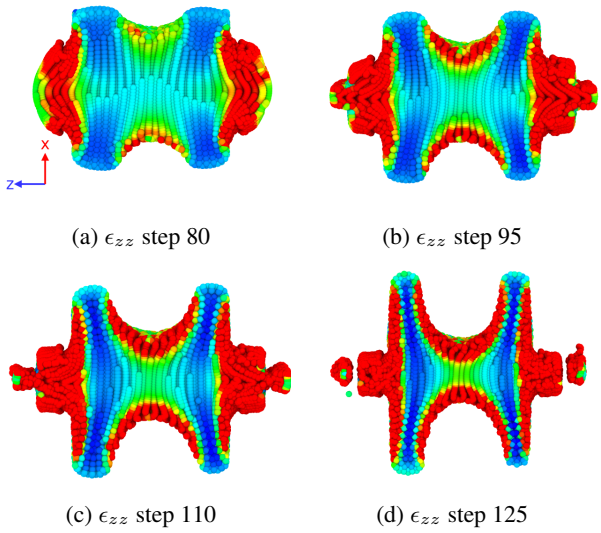

(a) ϵ_{zz} step 80 (b) ϵ_{zz} step 95

(c) ϵ_{zz} step 110 (d) ϵ_{zz} step 125

Figure 22: Relative ϵ_{zz}: [-0.1 $\rightarrow$ 0.1] along crankshaft axis z in thickest cross section (view along y axis).

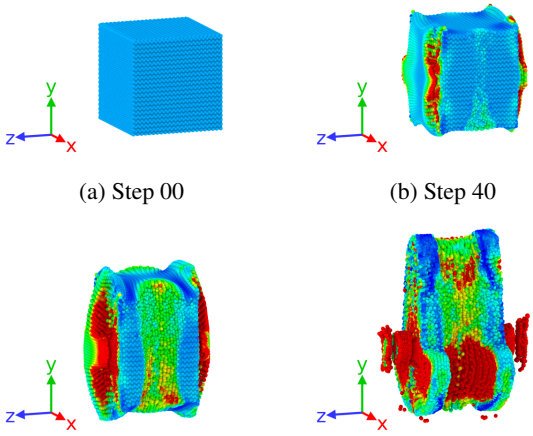

(a) Step 00 (b) Step 40

(c) Step 80 (d) Step 125

Figure 21: Oblique top view of the evolution of ϵ_{zz}: [-0.1 $\rightarrow$ 0.1].

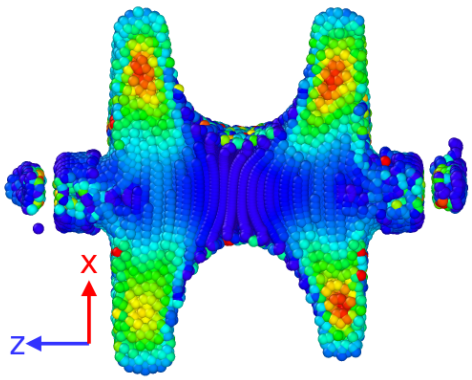

Figure 23: Relative ϵ_{xx}: [-0.1 $\rightarrow$ 0.1] at step 125 in thickest cross section.

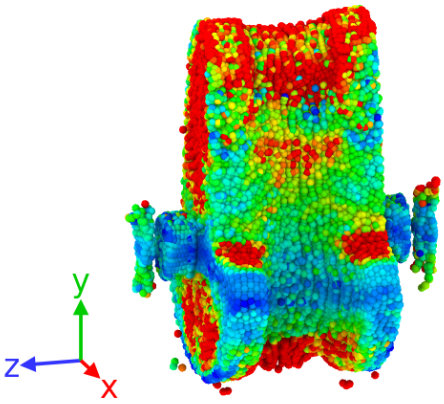

Figure 24: Relative ϵ_{yy}: [-0.1 $\rightarrow$ 0.1] at step 125 (top view).

clipping plane through the counterweight section, chosen to include the main (central) bearing. There is global deformation throughout the billet with the greatest material flow occuring in the deepest part of the die fig. 20d. A similar view of the process is given in fig. 21 where the surface is painted with the strain along the main axis. The increase in the strain around the central bearing and throughout the region between the counterweights is clearly visible fig. 21d. The evolution of ϵ_{zz} throughout the interior of the crankunit, in its thickest part, is given in fig. 22. Here the effects around the central bearing and near the surface between the counterweights are further emphasized 22d.

The effect of the forging process on the thickest features of the part are highlighted in fig. 23 where ϵ_{xx} is shown. One sees that the strain in this region is aligned with the axis of die motion. Finally the strain along the longest part dimension (direction of crank offset) is shown fig. 24. The strain is maximized near the parting line and toward the connecting rod bearing where the die is most shallow.

4 Discussion

Overall the simulations provided stable and credible results for the cases under study. The predicted deformations helped in identifying problem areas such as billet fracturing and incomplete die filling (data not shown) so that the test cases could be optimized. In some cases, however, the simulation parameters needed to be modified to adapt to the nuances of each case.

4.1 Effect of Simulation Parameters

Update frequency and contact stiffness had the greatest impact on the trajectories. The contact stiffness was increased to compensate for the stiffness of steel so the billet would not penetrate the die surface. The reference frame update and smoothing kernel radius influenced the output of the highest plasticity cases, namely the seamless pipe extrusion and the four arm extrusion (discussed below). Decreased particle size was also investigated (data not shown), but not surprisingly, was found to have a cubic impact the on simulation time.

4.1.1 Effect of Update Frequency

In order to handle large plastic deformations and maintain simulation stability [14], the initial configuration of the system was reset when the displacement of any one particle exceeded a tunable displacement criteria. The reset criteria occured when the displacement between any two particles exceeded 50 percent of the smoothing radius. This was notable in regions of high shear where the particle registry (contact topology) would change. When this threshold was exceeded, the initial configuration for *all* billet particles was reset to the current positions. The update would affect the cumulative strain but (by design) leave the stress and plastic deformation history intact. The part geometry and configuration of the forging system also had an impact on these updates. For instance, the yoke and crank-throw experienced few updates, while the seamless pipe and four arm part experienced several updates; the material flow in these latter cases being more complex. The reverse extrusion had shear bands where particles were disconnected from their neighbors by the punch action, similar to a cutting tool. Here, the effects were most apparent on the inner wall of the extruded pipe. The flow pattern within the four arm die exhibited diverted flows and flow through constrictions. Within these regions the particles would shear past each other so the configuration would frequently be reset.

When the particles were reset, the strain would also be reset. To get a sense for the overall strain, the Lammps [7] platform and the SMD implementation [6] were altered to compute a *cumulative* strain based on the initial state of the trajectory. Even though this strain was invalid around the areas where the reset criteria triggered, it nonetheless gave an indication of the overall deformation. To facilitate the display, the determinant of the deformation matrix $\mathbf{F}$ was output (in the dump data) and used to filter out particles [13] where the determinant was either negative or assumed excessive values.

4.2 Effect of Physical Parameters

The higher temperature case required lower average die forces as expected, compare figs. 15, 18. This can be understood from the data given in [12], which shows a 20 fold reduction in billet stiffness for the higher temperature. Also apparent was the greater material flow due to the lower yield stress.

4.3 Summary of Effects of Die Geometry

The simulations where the range of punch motion relative to the maximum billet extent was smallest seemed to be the best behaved. In these cases, the number of reference

state resets was minimal. When the punch motion was along the longest axis of the billet, however, the reference state had to be reset many times. Also, it was noted in the 4arm case, that the billet would undergo large compressive deformation before actually flowing into the lateral die spaces. This was surprising considering the relative incompressibility of steel, even at high temperatures. This anomaly is probably due to a simplistic constitutive model and could be remedied by modeling incompressibility.

5 Conclusion

The Lammps implementation of Smooth Mach Dynamics was used to simulate four representative non-trivial metal forging operations. The cases covered a wide spectrum of material deformation and forging die geometry. The Total Lagrangian method provided credible predictions of the deformation process and proved useful in identifying problems occuring in the design of forging processes.

References

[1] J.R. Cho, D.Y. Yang, Three-dimensional finite element simulation of a spider hot forging process using a new remeshing scheme, *J. Mater. Process. Technol. 99* (2000) 219–225.

[2] G. Li, T. Belytschko, Element free Galerkin method for contact problems in metal forming analysis, *Eng. Comput. 18* (2000) 62–78.

[3] P.W. Cleary, M. Prakash, J. Ha, Novel applications of Smoothed Particle Hydrodynamics (SPH) in metal forming, *J. Mater. Process. Technol. 177* (1–3) (2006) 41–48.

[4] Belytschko, T., Guo, Y., Liu, W.K., Xiao, S.P., 2000. A unified stability analysis of meshless particle methods. *Int. J. Numer. Methods Eng. 48* (9), 1359–1400.

[5] Bonet, J., Kulasegaram, S., 2001. Remarks on tension instability of Eulerian and lagrangian corrected smooth particle hydrodynamics (CSPH) methods. *Int. J. Numer. Methods Eng. 52* (11), 1203–1220.

[6] Ganzenmüller, G.C., 2015. An hourglass control algorithm for lagrangian smooth particle hydrodynamics. *Comput. Methods Appl. Mech. Eng. 286*, 87–106.

[7] Plimpton, S., Crozier, P. and Thompson, A., 2007. LAMMPS-large-scale atomic/molecular massively parallel simulator. *Sandia National Laboratories, 18*, p.43.

[8] Wilkins, J.L. Calculation of elastic-plastic flow: *Methods of Computational Physics, Academic Press*, New York, 1964, pp 211-263.

[9] Leroch, S., Varga, M., Eder, S.J., Vernes, A., Ripoll, M.R. and Ganzenmüller, G., 2016. Smooth particle hydrodynamics simulation of damage induced by a spherical indenter scratching a viscoplastic material. *International Journal of Solids and Structures, 81*, pp.188-202.

[10] Cleary, P.W., Prakash, M., Das, R. and Ha, J., 2012. Modelling of metal forging using SPH. *Applied Mathematical Modelling, 36*(8), pp.3836-3855.

[11] Ribés, A. and Bruneton, A., 2014, November. Visualizing results in the SALOME platform for large numerical simulations: an integration of ParaView. *2014 IEEE 4th Symposium on Large Data Analysis and Visualization* (pp. 119-120).

[12] Outinen, J. and Mäkeläinen, P., 2004. Mechanical properties of structural steel at elevated temperatures and after cooling down. *Fire and materials, 28*(2-4), pp.237-251.

[13] Stukowski, A., 2009. Visualization and analysis of atomistic simulation data with OVITO–the Open Visualization Tool. *Modelling and Simulation in Materials Science and Engineering, 18*(1), p.015012.

[14] Islam, M.R.I. and Peng, C., 2019. A stabilized total-Lagrangian SPH method for large deformation and failure in geomaterials. *IarXiv* preprint arXiv:1907.06990.

6 Appendix A

The algorithm for computing equations of motion of SMD particles due to stress forces from [9] is given here along with the steps needed for reference frame reset (ie. implicit remeshing).

Algorithm 1 Verlet algorithm for equations of motion

procedure MAIN LOOP(t_{total}) ▷ Main Loop of Equations of Motion
  while $t \leq t_{total}$ **do** ▷ run simulation for time interval
    for all i **do** ▷ loop over all particles
      $\mathbf{v}_i \leftarrow \mathbf{v}_i + \frac{1}{2m_i}\Delta t \mathbf{f}_i$ ▷ compute velocity
      $\mathbf{x}_i \leftarrow \mathbf{x}_i + \Delta t \mathbf{v}_i$ ▷ compute new position
      for all $j \in S_i$ **do** ▷ loop over all particles j in neighborhood of particle i
        $r_{ij} \leftarrow |\mathbf{x}_i - \mathbf{x}_j|$ ▷ Compute distance from particle i to j
        $r^0_{ij} \leftarrow |\mathbf{X}_i - \mathbf{X}_j|$ ▷ Compute reference distance from particle i to j
        if $r_{ij} - r^0_{ij} > ThresHold$ **then** ▷ If distance exceeds reference distance by tunable threshold
          $UpdateFlag \leftarrow 1$ ▷ Set flag to update material frame
    if $UpdateFlag$ **then**
      for all i **do** ▷ loop over all particles
        $\mathbf{X}_i \leftarrow \mathbf{x}_i$ ▷ Update reference positions
    for all i **do** ▷ loop over all particles
      $\mathbf{F}_i \leftarrow \mathbf{0}$ ▷ initialize deformation tensor
      $\dot{\mathbf{F}}_i \leftarrow \mathbf{0}$ ▷ initialize deformation rate tensor
      $\mathbf{K}_i \leftarrow \mathbf{0}$ ▷ initialize shape normalization tensor
      for all $j \in S_i$ **do** ▷ loop over all neighbors of particle i
        $\mathbf{F}_i \leftarrow \mathbf{F}_i + V^0_j \mathbf{x}_{ij} \otimes \nabla W(X_{ij})$ ▷ update deformation tensor i from particle j
        $\dot{\mathbf{F}}_i \leftarrow \dot{\mathbf{F}}_i + V^0_j \mathbf{v}_{ij} \otimes \nabla W(X_{ij})$ ▷ update deformation rate tensor i from particle j
        $\mathbf{K}_i \leftarrow \mathbf{K}_i + V^0_j \mathbf{X}_{ij} \otimes \nabla W(X_{ij})$ ▷ update shape normalization tensor i from particle j
      $\mathbf{F}_i \leftarrow \mathbf{F}_i \mathbf{K}_i^{-1}$ ▷ compute corrected deformation tensor
      $\dot{\mathbf{F}}_i \leftarrow \dot{\mathbf{F}}_i \mathbf{K}_i^{-1}$ ▷ compute corrected deformation rate tensor
      $\mathbf{L}_i \leftarrow \dot{\mathbf{F}}_i \mathbf{F}_i^{-1}$ ▷ compute velocity gradient
      $\mathbf{D}_i \leftarrow \frac{1}{2}(\mathbf{L}_i + \mathbf{L}_i^T)$ ▷ compute strain rate tensor
      $\mathbf{R}_i \mathbf{U}_i \leftarrow \mathbf{F}_i$ ▷ compute polar decomposition of **F** into **R** and **U** parts
      $\mathbf{d}_i \leftarrow \mathbf{R}_i^T \mathbf{D}_i \mathbf{R}_i$ ▷ subtract rigid rotations from strain rate tensor
      $\dot{\sigma}'_i \leftarrow C(\mathbf{d}_i)$ ▷ compute unrotated stress using constitutive model C
      $\sigma'_i \leftarrow \sigma'_i + \Delta t \dot{\sigma}'_i$ ▷ compute unrotated stress using constitutive model C
      $\sigma_i \leftarrow \mathbf{R}_i \sigma'_i \mathbf{R}_i^T$ ▷ rotate unrotated stress to current coordinates
      $\mathbf{P}_i \leftarrow J \sigma_i \mathbf{F}_i^{-T}$ ▷ compute Piola Kirchoff Stress
    for all i **do** ▷ loop over all particles
      $\mathbf{f}_i \leftarrow \mathbf{0}$ ▷ initialize force vector
      for all $j \in S_i$ **do** ▷ loop over all neighbors of particle i
        $\mathbf{f}_i \leftarrow \mathbf{f}_i + V^0_i V^0_j (\mathbf{P}_i \mathbf{K}_i^{-1} + \mathbf{P}_j \mathbf{K}_i^{-1}) \nabla W(X_{ij}))$ ▷ sum stress force contributions
        $\mathbf{f}_i \leftarrow \mathbf{f}_i + \mathbf{f}^{HG}_{ij}$ ▷ add in hourglass force
    for all i **do** ▷ loop over all particles
      $\mathbf{v}_i \leftarrow \mathbf{v}_i + \frac{1}{2m_i}\Delta t \mathbf{f}_i$ ▷ compute velocity
    $t \leftarrow t + \Delta t$ ▷ increment time

The radial return algorithm used to handle plastic flow.

Algorithm 2 Radial return algorithm for handling plastic deformations

procedure PLASTICITY ALGORITHM(t_{total}) ▷ Radial return plasticity algorithm
  $\sigma_d^{trial} \leftarrow s\sigma_d^n + 2G\Delta t\mathbf{d}_d$ ▷ elastic stress update
  $J_2^{trial} \leftarrow \sqrt{\frac{2}{3}\sigma_d^{trial} : \sigma_d^{trial}}$ ▷ J2 norm of deviatoric stress
  if $J_2^{trial} < \sigma_y$ **then**
    $\sigma_d^{n+1} \leftarrow \sigma_d^{trial}$ ▷ Yield stress not exceeded keep elastic update
  else
    $\delta\epsilon \leftarrow \frac{J_2^{trial} - \sigma_y}{3G}$ ▷ Compute plastic strain for this timestep
    $\epsilon^{n+1} \leftarrow \epsilon^n + \Delta\epsilon$ ▷ increment plastic strain
    $\sigma_d^{n+1} \leftarrow \frac{\sigma_y}{J_2^{trial}}\sigma_d^{trial}$ ▷ scale deviatoric stress back onto yield surface